



**HAL**  
open science

# Coupling statistical indentation and microscopy to evaluate micromechanical properties of materials: Application to viscoelastic behavior of irradiated mortars

Benoit Hilloulin, Maxime Robira, Ahmed Loukili

► **To cite this version:**

Benoit Hilloulin, Maxime Robira, Ahmed Loukili. Coupling statistical indentation and microscopy to evaluate micromechanical properties of materials: Application to viscoelastic behavior of irradiated mortars. *Cement and Concrete Composites*, 2018, 94, pp.153 - 165. 10.1016/j.cemconcomp.2018.09.008 . hal-01938271

**HAL Id: hal-01938271**

**<https://hal.science/hal-01938271>**

Submitted on 28 Nov 2018

**HAL** is a multi-disciplinary open access archive for the deposit and dissemination of scientific research documents, whether they are published or not. The documents may come from teaching and research institutions in France or abroad, or from public or private research centers.

L'archive ouverte pluridisciplinaire **HAL**, est destinée au dépôt et à la diffusion de documents scientifiques de niveau recherche, publiés ou non, émanant des établissements d'enseignement et de recherche français ou étrangers, des laboratoires publics ou privés.

1           **Coupling statistical indentation and microscopy to evaluate micromechanical**  
2           **properties of materials: application to viscoelastic behavior of irradiated mortars**

3                           Benoit Hilloulin<sup>a\*</sup>, Maxime Robira<sup>a,b,c</sup>, Ahmed Loukili<sup>a</sup>

4           <sup>a</sup>, *Institut de Recherche en Génie Civil et Mécanique (GeM), UMR-CNRS 6183, Ecole Centrale*  
5           *de Nantes, 1 rue de la Noë, 44321 Nantes, France – e-mail: benoit.hilloulin@ec-nantes.fr;*  
6           *ahmed.loukili@ec-nantes.fr*

7           <sup>b</sup> *SUBATECH, Unité Mixte de Recherche 6457, École des Mines de Nantes, CNRS/IN2P3,*  
8           *Université de Nantes, BP 20722, 44307 Nantes cedex 3, France – e-mail:*  
9           *robira@subatech.in2p3.fr*

10          <sup>c</sup> *Tractebel Engineering – Le Delage, 5 rue du 19 Mars 1962, 92622 Gennevilliers CEDEX,*  
11          *France*

12  
13  
14          \* Corresponding author: Tel.: + 33 (0)2 40 37 16 61

15  
16  
17          **Highlights**

18          - Data mining principles applied to materials can lead to substantial improvements in  
19          the properties identification process.

20          - Coupling indentation and optical analysis reduces identified phase properties'  
21          variability.

22          -  $\gamma$ -irradiated mortar samples exhibit greater creep modulus and hardness and lower  
23          creep characteristic time than references.

24

25 **Abstract**

26 In this work, an original method coupling statistical indentation and 3D microscope  
27 image analysis for heterogenous materials characterization is developed. Statistical  
28 microindentation test results performed on  $\gamma$ -irradiated and pristine mortar specimens  
29 are presented and analyzed using a clustering data mining technique. The outputs are  
30 compared with the phase identification from 3D image analysis to effectively reduce  
31 uncertainties in the material properties of one of the phases (cement paste). With respect  
32 to the effects of irradiations on cementitious materials, a significant increase of cement  
33 paste creep modulus and hardness, and a significant decrease of creep characteristic  
34 time, are highlighted after an exposition of 257 kGy at 8.5 Gy /min. Young's modulus  
35 of the cement paste is not significantly affected. These results confirm macroscopic  
36 concrete creep observations presented in previous studies fitted with dose-dependent  
37 logarithmic laws.

38  
39  
40 **Keywords:** Indentation, Cement Paste (D), Mechanical properties (C), Creep (C),  
41 Radioactive Waste (E), Image analysis (B).

42  
43 **1. Introduction**

44 The macroscopic mechanical properties of concrete mainly depend on micro-  
45 mechanical properties of its binding phase (i.e., the cement paste) and more particularly  
46 on the calcium silicate hydrate (CSH) gel, which exhibits significant local variations.  
47 For some years, microindentation and nanoindentation have been widely investigated to  
48 characterize elasto-plastic and creep properties of cementitious materials [1-4].

49 Indentation elastic parameters can then be input in homogenization schemes to  
50 determine concrete elastic properties [5-7].

51 According to Oliver and Pharr theory [8], the initial elastic unloading part of indentation  
52 curves can be analyzed to determine the indentation modulus and the indentation  
53 hardness of homogenous materials. Because cement paste is highly heterogenous, even  
54 at very small length scales, statistical nanoindentation performed at loads leading to  
55 penetration depths of some hundreds of nanometers has been developed. Assuming  
56 several phases may be indented at the same time, statistical indentation's main objective  
57 is to collect enough data points to apply a deconvolution algorithm giving the individual  
58 phase properties [9, 10]. However, two main critical aspects were identified regarding  
59 the application of statistical indentation technique to cementitious materials [11]: the  
60 size of the interaction volume may be larger than the size of the single phases at the risk  
61 of creating spurious peaks in the probability density function (PDF) [12, 13] as well as  
62 micromechanical values depending on the applied load [14], and the deconvolution  
63 analysis based on Gaussian Mixture itself may converge to local minima [15].  
64 Therefore, coupling indentation results to other techniques identifying the effective  
65 nature of the indents is of great interest at different scales: using atomic force  
66 microscope [16] or SEM [6, 17, 18]. Coupling nanoindentation and SEM-EDS to filter  
67 data points, Chen et al. highlighted the presence of ultra-high density CSH/Ca(OH)<sub>2</sub>  
68 nanocomposites in low water-to-cement ratio cement paste by correlating  
69 micromechanical properties, e.g. indentation hardness or indentation modulus, to the  
70 portlandite volume fraction measured in volumes with approximately the same size as  
71 the one investigated through nanoindentation. Localization of indents by imaging  
72 techniques can also be used to differentiate the properties of several inclusions [19, 20]  
73 and eventually map a restricted area depending on the measured mechanical properties

74 [19, 21]. From the microscale to the macroscale, 3D image analysis of concrete or  
75 mortar surface appears to offer a promising field of research for purposes of generating  
76 geometric or topological data and supplementing other experimental techniques or  
77 providing input for numerical models [22-24].

78 Besides these developments concerning statistical indentation and imaging, it has been  
79 found out that the long-term creep properties of concrete specimens are related to the  
80 creep properties measured during minute-long microindentation or nanoindentation  
81 experiments. Both creep behaviors can be described using logarithmic time-dependent  
82 functions with two main variables: creep modulus and creep characteristic time [7, 25,  
83 26]. Creep modulus of cement paste is linearly correlated with indentation hardness  
84 which means that the lower the hardness, the greater the creep strains, though the slope  
85 of the regression depends on the material: creep modulus of pure CSH is greater than  
86 the one of cement paste and it decreases with Ca/Si ratio [27]. Like macroscopic creep,  
87 indentation creep depends on the relative humidity [28].

88 In the context of nuclear waste disposals and, more generally, in the scope of nuclear  
89 safety structures characterization, the assessment of mechanical properties of irradiated  
90 concrete is of great interest to speculate over long term behavior of concrete under  
91 irradiations. Concrete properties evolutions with radiations have recently been  
92 summarized [29]. An extensive literature review ensures that irradiations lead to a  
93 decrease of the macroscopic strength of concrete under several types of radiations ( $\alpha$ ,  $\gamma$   
94 and neutrons). The main mechanism behind concrete degradation under  $\alpha$ -radiation is  
95 radiation-induced volumetric expansion (RIVE) of siliceous aggregates [30, 31] at doses  
96 greater than a reference dose of around  $1 \times 10^{20}$  n/cm<sup>2</sup> [32]. But under pure  $\gamma$ -radiation  
97 (exposition condition of structural concrete element of disposals [33]), degradation  
98 mechanisms are not understood yet and there is still a debate whether a reference level

99 of  $2 \times 10^5$  kGy introduced some decades ago is relevant or not as some recent studies  
100 showed degradations after the exposure to lower doses [34, 35]. Water radiolysis  
101 triggered by  $\gamma$ -radiation is supposed to be the main phenomenon responsible of possible  
102 degradations located in the cement paste [36, 37] and phase alterations occurs only at  
103 very high doses of some dozens or even hundreds of MGy [38]. Concrete creep under  
104 low dose irradiation ( $< 1$  Gy / h [33]) is one of the major preoccupations concerning  
105 long-term behavior of waste disposal infrastructures. To our knowledge, only one study  
106 reported the smaller extent of creep of  $\gamma$ -irradiated concrete under compression, though  
107 measurements were carried out over a relatively short period of one year without any  
108 repetition [39].

109 The growing use of various data mining techniques in civil engineering and materials  
110 science applications is changing the way scientists and engineers are facing issues and  
111 creating promising paths of investigation at the same time. Larger datasets can be  
112 obtained and the challenge is to find useful and innovative information out of them [40].  
113 Data mining techniques are being developed to identify materials properties [41] and  
114 even leading to the creation of novel materials. In civil engineering [42], data mining  
115 has mainly been used for large scale transportation problems for some years [43].

116 A main objective of the present work is to demonstrate the potential of data mining  
117 techniques for material properties identification in civil engineering at a microscale and  
118 mesoscale, at the crossroads of materials science and civil engineering. For this purpose,  
119 two complementary methods, namely statistical microindentation and microscopy, were  
120 performed on mortar specimens and combined to detect hidden data trends. Used  
121 together with adequate data mining techniques, microindentation data analysis and  
122 optical microscopy image analysis are shown to reduce the uncertainties associated with  
123 cement paste mechanical properties identification. An application to the determination

124 of mechanical properties of  $\gamma$ -irradiated mortars is then proposed. The first micro  
125 mechanical dataset of this type is reported and compared with the only, because tedious,  
126 measurement performed on concrete some decades ago [39]. Hundreds of measurement  
127 points obtained from 3 irradiated and 3 pristine control specimens are compared to  
128 highlight hidden trends due to radiation exposure.

129

## 130 **2. Materials and methods**

### 131 **2.1 Specimens preparation and irradiation conditions**

132 Mortar was prepared with CEM I 52.5 and 0/4 mm calcareous sand (to avoid the  
133 activation of alkali-silica reaction by irradiation) with the proportions detailed in  
134 Table 1. Any use of organic additives like superplasticizer or demolding oil was  
135 avoided to not induce a possible premature degradation by the irradiations. This mortar  
136 formulation was determined to be as representative as possible of a high-performance  
137 concrete used in nuclear waste storage facility galleries.

138 Six mortar prisms with dimensions of 4 x 4 x 16 cm<sup>3</sup> were cast in polypropylene molds  
139 to avoid any presence of metallic compounds from the molds. After 1 day of curing  
140 under sealed conditions in an air-conditioned room at a temperature of 20°C and  
141 90% RH, the specimens were demolded. The specimens were further cured in lime-  
142 saturated water until the age of 28 days. Mortar prisms were then dried during 14 days  
143 in an oven at 45°C (a constant mass was measured at 10 days).

144 Half of the mortar prisms (MD-257kGy-I1 to MD-257kGy-I3) were then introduced in  
145 an irradiator at ARRONAX (<sup>137</sup>Cs source, 661 keV, 123.4 TBq) at the age of 42 days.  
146 Specimens were exposed as close to the source as possible to guarantee a spatially  
147 homogenous dosage during 3 weeks. The total  $\gamma$  dose received by the specimens was  
148 calculated to be around 257 kGy based on a map of the  $\gamma$  fluxes in the irradiator realized

149 by Fricke dosimetry measurement. The other half of the specimens (MD-257kGy-S1 to  
150 MD-257kGy-S3), e.g. the control specimens, were kept in an air-conditioned room at  
151 relative humidity of around 65% close to the ones measured in the irradiator at the end  
152 of the irradiation period.

153 **Table 1.** Mortar compositions

Cement (kg/m <sup>3</sup> )	Calcareous Sand 0/4 (kg/m <sup>3</sup> )	Water (kg/m <sup>3</sup> )	W/C	Paste volume (%)
566	1344	270	0.43	45

154  
155 Several mechanical and chemo-physical tests were performed on these mortars and on  
156 other series as well. The results will be presented in future communications but, in the  
157 sake of clarity, some results may be evocated in regards to micromechanical results  
158 presented herein. No evident carbonation, pore size evolution or hydrated phases  
159 transformations were measured. Thus micromechanical properties evolutions may not  
160 be attributed to calcite formation in contrast with [44].

161

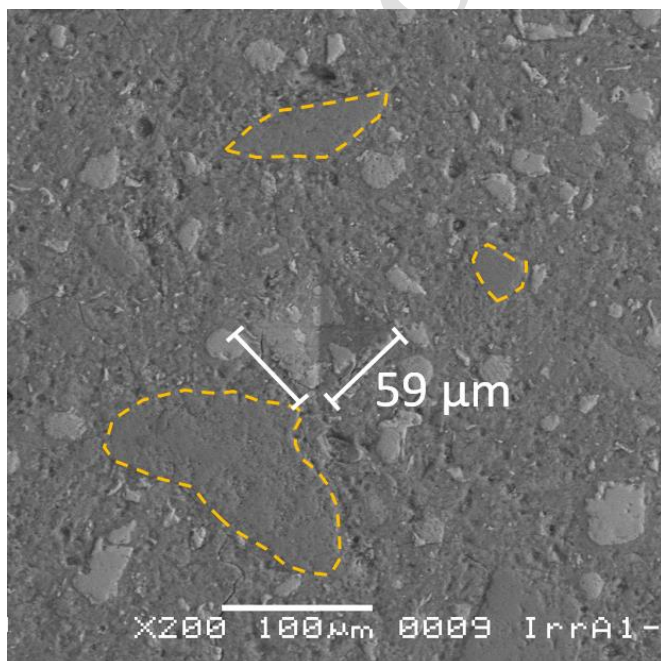
## 162 **2.2 Indentation setup and theory**

163 Microindentation tests were performed during the week following the irradiation period  
164 with the main objective of comparing the properties of irradiated and control specimens.  
165 Thus, a volume of 2 x 2 x 1.5 cm<sup>3</sup> was sawn from the middle part of a half of the  
166 4 x 4 x 16 cm<sup>3</sup> broken by three-point bending test. This location was selected to avoid  
167 damage due to the three-point bending test. The 2 x 2 cm<sup>2</sup> section was polished with Si-  
168 C paper with decreasing particle size (500, 1200, 2000, 4000) using ethanol as polishing  
169 liquid. Polishing times were selected around some minutes per paper to limit the risk of  
170 aggregate cracking. These times are much shorter than the ones used for

171 nanoindentation on cement pastes [45] but were sufficient to obtain a surface roughness  
172  $R_q$  of around 0.5 - 1  $\mu\text{m}$  which is acceptable for micro-indentation with penetration  
173 depth of some microns.

174 A typical cement paste area with a typical indent is presented in Fig. 1. As it can be  
175 observed, the scale of the indent is larger than the characteristic scale of the  
176 microstructure of the cement paste (residual anhydrous clinker size): thus, the  
177 performed microindentation tests provided the mechanical properties of the cement  
178 paste or the sand, or the interface and not of the individual phases of the cement paste.

179 Microindentation was performed using a Vickers indenter probe over a grid of  
180 20 x 20 points, evenly spaced by 500  $\mu\text{m}$  to investigate a representative surface of  
181 1 x 1  $\text{cm}^2$  of the mortar sample. For each indent, the load was increased linearly over  
182 time in 5 s up to 2000 mN, kept constant during the 60 s holding phase, and decreased  
183 linearly over time back to zero in 5 s. The very short loading time was selected to limit  
184 creep during this period and do not apparently damaged the sample.



185 **Fig. 1.** SEM observation of a typical indent located in the cement paste with a width of  
186 59  $\mu\text{m}$  (small sand fines located near the indent are circled by orange dashed lines).

187

188 Various properties were calculated from the load – penetration curves. First, the  
189 indentation hardness depending on the maximum load and the projected contact area:

$$H_{IT} = \frac{P_{max}}{A_p(h_c)} \quad (1)$$

190 For Vickers' indenter the projected contact area can be estimated by:

$$A_p(h_c) = 24.50h_c^2 \quad (2)$$

191 Where  $h_c$  can be calculated based on maximum indentation depth  $h_{max}$  assuming:

$$h_c = h_{max} - \varepsilon(h_{max} - h_r) \quad (3)$$

192 with  $\varepsilon = 0.75$  and  $h_r$  is the final ideal penetration height can be determined. Martens  
193 hardness was also computed according to:

$$H_M = \frac{P_{max}}{A_s(h)} \quad (4)$$

194 Where  $A_s(h)$  is the contact area, depending on the indentation depth  $h$ , defined for a  
195 Vickers indenter by:

$$A_s(h) = \frac{4 \sin(\alpha/2)}{\cos^2(\alpha/2)} h^2 \approx 26.43h^2 \quad (5)$$

196 With  $\alpha=136^\circ$  the top angle of the Vickers pyramid.

197 The Young's modulus  $E_{IT}$  of the indented material is given by:

$$M = \frac{E_{IT}}{1 - \nu_s^2} = \frac{1}{\frac{1}{E_r} - \frac{1}{M_{ind}}} \quad (6)$$

198 Where  $M$  denotes the indentation modulus,  $M_{ind} = 1140 \text{ GPa}$  the modulus of the  
199 indenter,  $\nu_s$  the Poisson ratio of the material (considered equal to 0.2, a possible

200 variation of some percent of EIT may be induced for other values of Poisson ratio) and  
 201  $E_r$  is the reduced modulus which is determined assuming:

$$E_r = \frac{1}{2} \left( \frac{dP}{dh} \sqrt{\frac{\pi}{A}} \right) \text{ at } h = h_{max} \quad (7)$$

202 A first creep parameter  $C_{IT}$ , e.g. the normalized indentation creep parameter, was  
 203 calculated by the machine. It is defined as:

$$C_{IT}(\%) = \frac{h_{max} - h_1}{h_1} \times 100 \quad (8)$$

204 With  $h_1$  the indentation depth at the beginning of the creep stage.

205 Energetic parameters  $n_{IT}$  and  $W_t$  were also recorded.  $n_{IT}$  is the proportion of the elastic  
 206 response relatively to the total energy  $W_t$ :  $n_{IT} = W_{elas} / W_t$ .

207 More meaningful creep parameters  $C$  and  $\tau$  can be extracted from the indentation curves  
 208 (see Fig 2a)) calculating the creep function  $L(t)$  [21]:

$$L(t) - L(0) = L(t) - \frac{1}{M} = \frac{2a_u \Delta h(t)}{P_{max}} \quad (9)$$

209 Where  $\Delta h(t)$  denotes the indentation depth increase during the constant load phase,  $a_u$   
 210 denotes the is the radius of the equivalent projected contact area between the indenter  
 211 probe and the indented surface at the onset of unloading

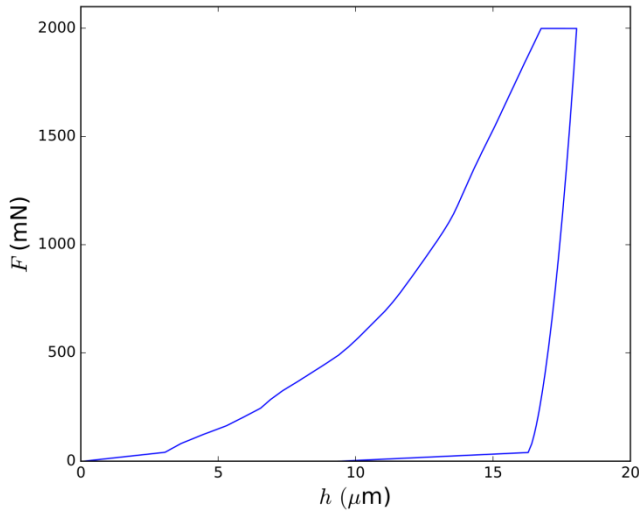
212 Assuming a logarithmic fit of the creep function, the creep parameters are defined  
 213 according to [25]:

$$L(t) - \frac{1}{M} = \frac{\ln(t/\tau + 1)}{C} \quad (10)$$

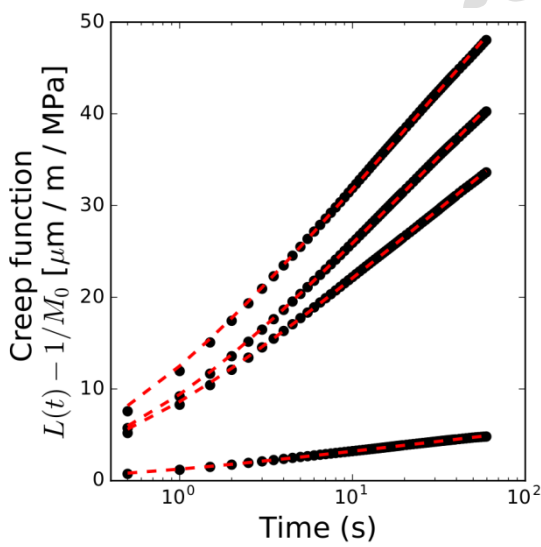
214 It was verified that this law can adequately reproduce the creep behavior of both cement  
 215 paste and sand as illustrated in Fig. 2 b). In order to avoid drying during creep  
 216 experiments, indentation was realized at a relative humidity close to the one imposed  
 217 during the irradiation period (around 65% RH). Moreover, autogenous shrinkage of the

218 sample can be neglected at the age of 72 d. Then, the creep function is expected to  
219 characterize the basic creep behavior of the specimens.  
220

a)



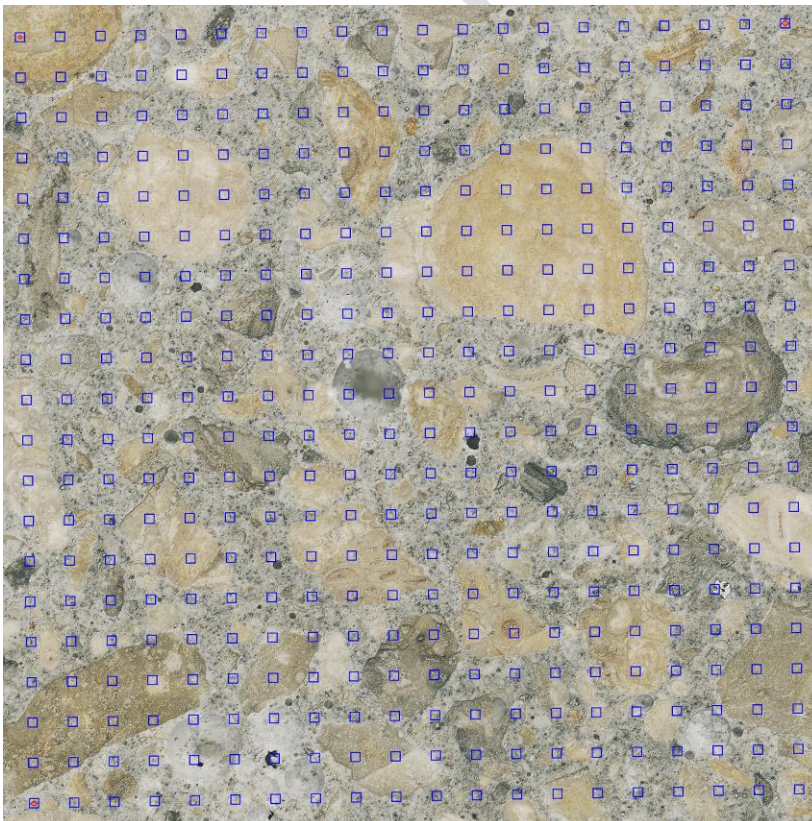
b)



221 **Fig. 2.** Microindentation outputs: a) raw load – penetration curve, b) fitting the creep  
222 function by a logarithmic law (3 curves correspond to cement paste indents and 1 to a  
223 sand indent)  
224

225 **2.3 3D microscope measurements and analysis**

226 After indentation, a map of the indented zone was realized using a Hirox RH-2000 3D  
227 microscope by merging around 200 3D reconstructed images evenly spaced along the  
228 indented area. The selected magnification (x 140) led to a final horizontal resolution of  
229 the 2D projected image of 1.5  $\mu\text{m}$  / pix which is adequate to correctly locate the indents  
230 and assess their nature. Because some indents may be hardly located, especially the  
231 ones created in voids, a basic routine was implemented in Python to locate all the  
232 indents based on the location of 3 of them by drawing blue squares on the original  
233 image. As illustrated in Fig. 3, the 20 x 20 matrix of indents covers a sufficiently large  
234 area representative of the mortar volume and the reconstructed image correctly  
235 represent the matrix without image distortion due to multiple image merging (it was  
236 verified that the indents were correctly located by the blue squares). The nature of the  
237 indents was then manually identified because color-based filters were found to be  
238 relatively imprecise in the case of such mortar images.



239

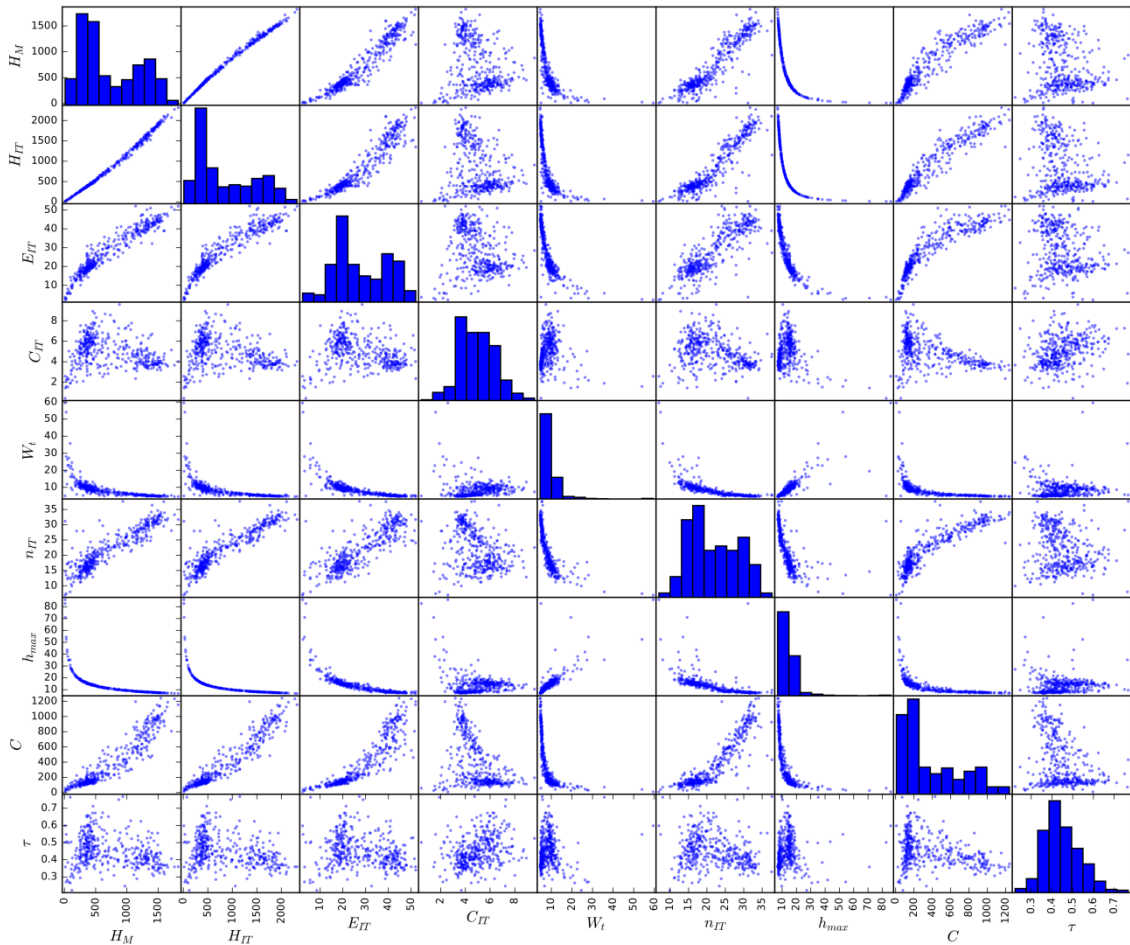
240 **Fig. 3.** 2D projected global view of the 20 x 20 matrix of indents over a 1 x 1 cm<sup>2</sup>  
241 surface from 3D microscope acquisition (indents are indicated by blue squares)

242

### 243 **3. Results and discussion**

#### 244 **3.1 Statistical indentation data deconvolution and its variability**

245 First, indentation outputs from each specimen were visualized by mean of a scatter plot  
246 as illustrated in Fig. 4. Several basic observations directly arise from the analysis of the  
247 scatter plot. Some data points are isolated from the others. These isolated points are  
248 mainly indents with a maximum penetration depth  $h_{\max}$  greater than 20  $\mu\text{m}$ . In order to  
249 properly run data deconvolution, these points were filtered out on all samples. As we  
250 will see in the next paragraph, they correspond to indents close to voids or local defects  
251 and therefore do not correctly represent cement paste properties. Due to sand  
252 heterogeneities, some data points exhibit indentation hardness greater than 2500 MPa.  
253 Such points were also filtered out of the analysis. Already reported correlations can be  
254 highlighted in the scatter plot: correlation between hardness and Young's modulus,  
255 linear-shaped correlation between hardness and creep modulus. Looking at the PDFs  
256 located along the diagonal of the scatter plots, one may also observe that two main  
257 groups, presumably the cement paste and the sand, can be identified (especially on  $H_{IT}$   
258 and  $E_{IT}$  PDFs). However, these two groups considerably overlap each over, probably  
259 due to a non-negligible proportion of the indents at the interface between cement paste  
260 and sand grains.



261

262 **Fig. 4.** Unfiltered scatter plot from sample MD-257kGy-S3 ( $H_M$  and  $H_{IT}$  are expressed  
 263 in MPa,  $E_{IT}$  and  $C$  in GPa,  $C_{IT}$  and  $n_{IT}$  in %,  $W_t$  in  $\mu\text{J}$ ,  $h_{\text{max}}$  in  $\mu\text{m}$  and  $\tau$  in s).

264 Then, data points repartition was visualized using a Euclidian distance-based  
 265 dendrogram generated from the 9 output variables as illustrated in Fig 5 a). This way,  
 266 the similarities between the data points can be highlighted without subjectivity  
 267 (subjectivity may come from the arbitrary choice of the number of clusters prior to  
 268 deconvolution, the output variables used to generate the clusters, e.g. typically 2 [9] or 3  
 269 [14] only). The data points mainly belong to two dissimilar groups joining at a high  
 270 around 60 and with their subgroups differentiated at highs around 20.

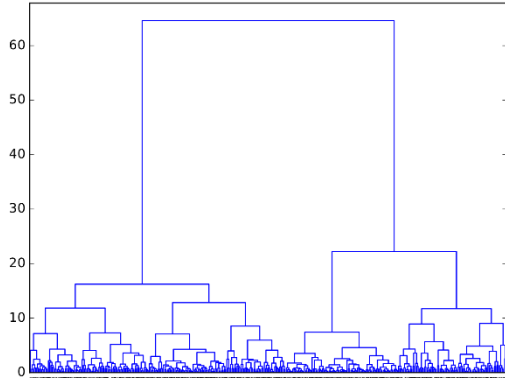
271 Cutting the dendrogram at a high of 30 leads to a 2-groups hierarchical clustering  
 272 represented on a  $C$ - $H_{IT}$  2D plane (Fig. 5 b)) with one group probably mainly composed  
 273 of cement paste and one group probably mainly composed of sand. Cutting the

274 dendrogram at a high of 20 leads to 3 groups (Fig. 5 c)). Naturally, because of  
275 hierarchical clustering principles, only one of the two groups has been divided into two  
276 subgroups, and for most of the mortar samples it is the group with the highest hardness  
277 (presumably sand indents). Then, it means that, at the selected indentation load, sand  
278 grains are more heterogeneous than the cement paste. It also leads to another  
279 observation: 2-groups (and 3-groups) hierarchical clustering clearly overestimates  
280 cement paste proportion, if one basically assumes that the group with the smallest mean  
281 hardness corresponds to the cement paste. Indeed, reading the dendrogram, the  
282 horizontal proportion of the first group corresponding to the lowest hardness is greater  
283 than the one of the second group corresponding to the highest hardness. As the  
284 horizontal axis is composed of all the single data points, it would mean that the number  
285 of indents in the cement paste is greater than the number of indents in the sand. That is a  
286 biased conclusion because the paste volume fraction is only of 45% (and at this  
287 indentation load, an important number of indents are located at the interface between  
288 cement paste and sand grains and they would lead to intermediate properties). This  
289 erroneous prediction of the phase volume fractions has already been reported elsewhere  
290 and the assignation of mean phases properties based on numerical data deconvolution is  
291 questionable [15]. This basic observation motivates the use of optical techniques  
292 described hereafter to filter experimental data based on indents nature.

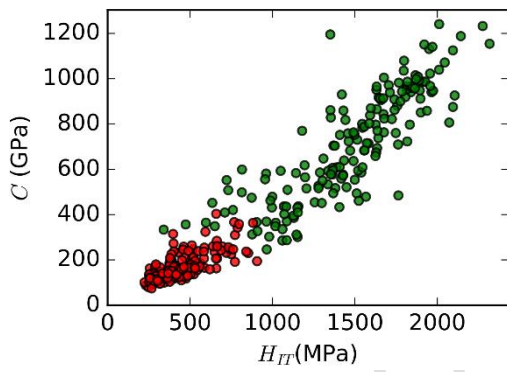
293 Reporting the nature of the indents predicted by deconvolution over the microscopic  
294 image as illustrated in Fig. 6, a relatively good correspondence is noticeable: red  
295 squares corresponding to the first deconvoluted group are mainly located in the paste  
296 and blue ones, corresponding to the second group are mainly located in sand grains,  
297 while black squares, corresponding to initially filtered values are all near voids.  
298 However, some indents (2 of them were circled in orange as examples) numerically

299 identified as cement paste are located on sand grains and vice versa which emphasizes  
300 the limits of numerical clustering.

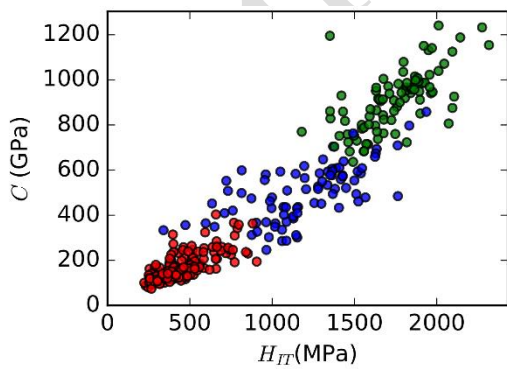
a)



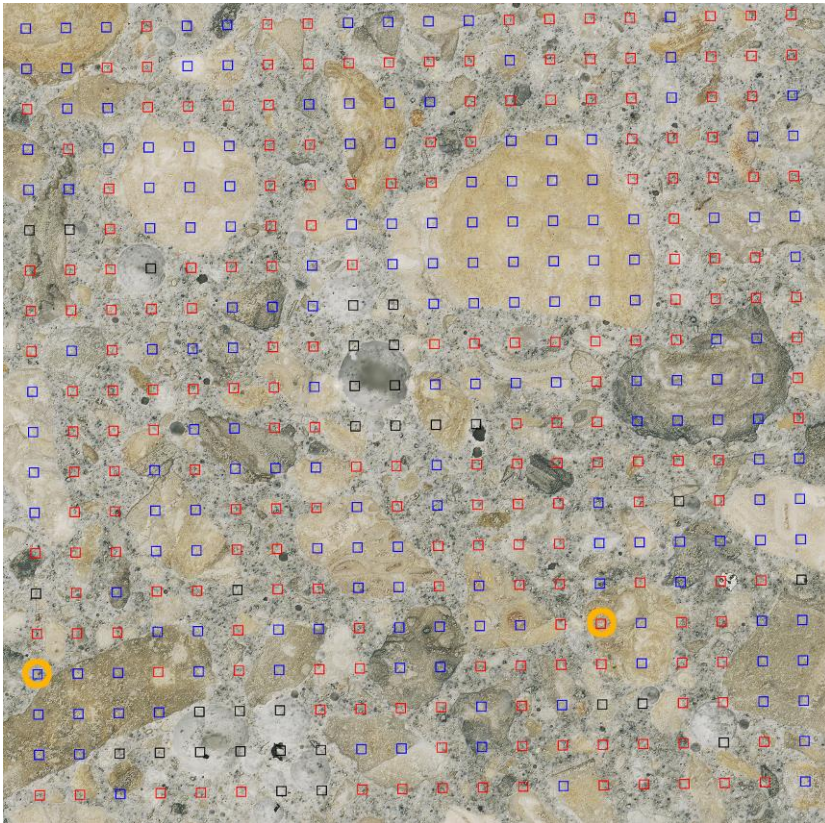
b)



c)



301 **Fig. 5.** Hierarchical clustering strategy applied to specimen MD-257kGy-S3: a)  
302 Euclidian distance-based dendrogram (with the 400 individual data points on the x-  
303 axis), b) and c), data points repartition along C- $H_{IT}$  plane using a 2-groups separation  
304 (b) and a 3-groups separation (c).



306

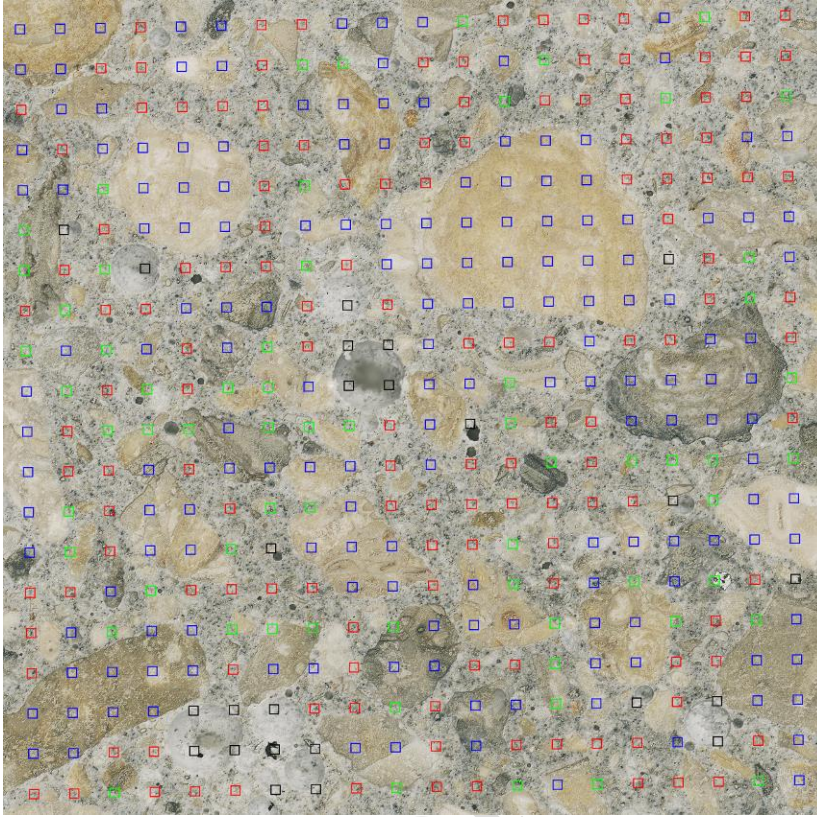
307 **Fig. 6.** Representation on the 3D microscopic image of specimen MD-257kGy-S3 of the  
 308 nature of the indents predicted by data deconvolution (red squares correspond to group  
 309 1, e.g. 'paste', blue squares to group 2, e.g. 'sand, and black squares to filtered values  
 310 before the analysis). Orange circles indicate two indents attributed to the wrong group  
 311 as an example of the limits of numerical clustering. Indentation area extends over  
 312  $1 \times 1\text{cm}^2$ .

313

### 314 3.2 3D microscope results

315 Indents were visually classified into 4 groups: voids, paste, sand and interface between  
 316 paste and sand so that the latter 3 could be compared to the 3 groups obtained by  
 317 hierarchical clustering. As illustrated in Fig. 7, there is an important proportion of  
 318 indents located at the cement paste - sand grains interface marked by green squares.  
 319 This is directly correlated to the indent size relatively to the size of the phase and the

320 volume fraction of sand. Comparing Fig. 6 with Fig. 7, one may notes that the other  
321 indents are on majority of the same nature as the indents attributed to one group using  
322 the hierarchical clustering method.

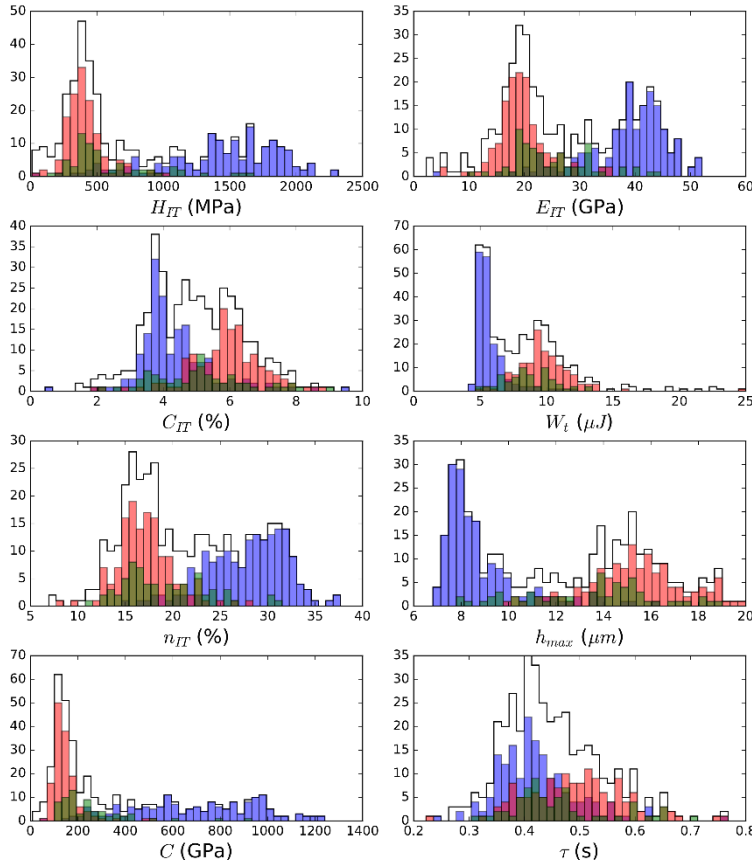


323  
324 **Fig. 7.** Indents location and nature of specimen MD-257kGy-S3 (paste in red, cement  
325 paste - sand grain interface in green, pure sand in blue, void in black) according the 3D  
326 microscope image analysis.

327  
328 From the repartition of the indented outputs variables per groups using 3D microscope  
329 (Fig. 8), it can be observed that cement paste and sand indentation variables  
330 distributions closely match normal distributions. On the other side, properties associated  
331 with indents located at interfaces between cement paste and sand grains (green  
332 histograms) are much more variables and do not follow any specific distribution. This is  
333 due to the fact that indents on interfaces could either exhibit the mean value when two  
334 phases properties are probed (for example there are a lot of indents on interfaces with

335 Young's modulus between 25 and 35 GPa, because this property is representative of a  
336 large volume), either be very similar to cement paste or sand properties because the  
337 indenter probe slide to one side during loading (most of the time, to the cement paste  
338 side because of its lower altitude). For this reason, a lot of indents on interfaces have an  
339 indentation hardness around 500 MPa, e.g. around the mean value of indents attributed  
340 to the cement paste as this property is representative of a smaller volume.

341 Identifying phases properties based on imaging is therefore possible for predominant  
342 phases like cement paste or sand. Distributions are well defined but some indents  
343 properties are possibly associated with the wrong group. For example, in Fig. 8, one can  
344 see that some indents with high hardness and creep modulus (around 1 GPa and  
345 400 GPa resp.) were identified as cement paste while some indents with Young's  
346 modulus lower than 15 GPa were identified as sand grains. More than half of these  
347 values are associated with either an odd indent shape on sand or the presence of very  
348 small sand grains close to an indent attributed to the cement paste (most of these indents  
349 are probably rightly on cement paste but the indentation variables may be influence by  
350 very close sand grains even under the indent). Thus, although the optical identification  
351 of the indents should be attractive and sufficient in some cases, the combination of a  
352 numerical deconvolution technique and of an imaging technique may help reduce the  
353 uncertainties concerning some minor odd indents outputs.



354

355 **Fig. 8.** Histograms of distributions of the indentation output variables of specimen MD-  
 356 257kGy-S3. Total distribution is represented by the continuous black line, distributions  
 357 of the phases identified using the 3D microscope are colored in red (cement paste), blue  
 358 (sand grains) and green (cement paste – sand grain interface).

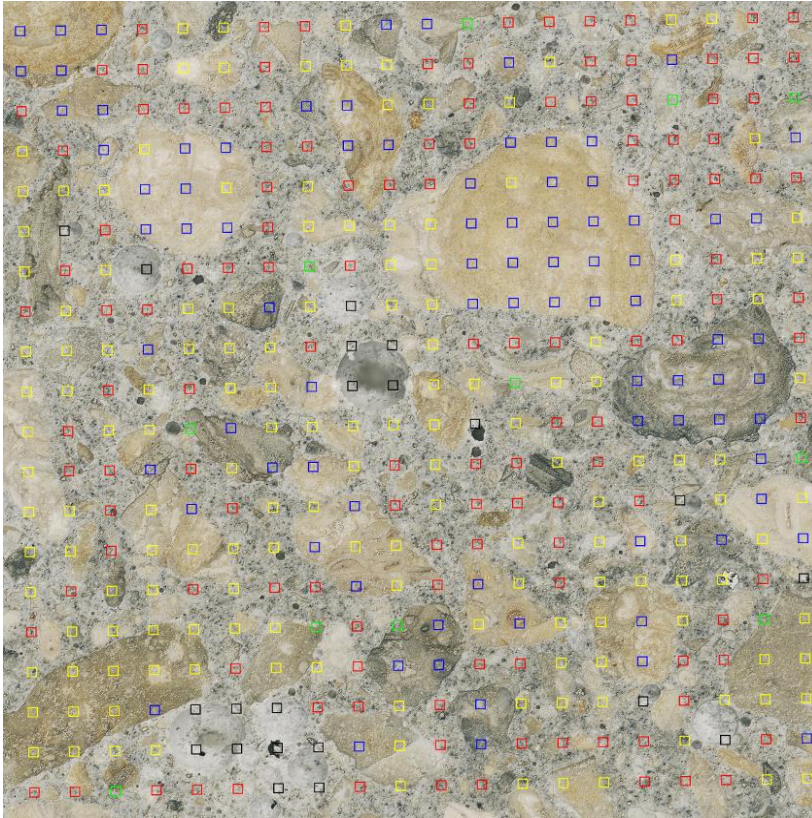
359

### 360 **3.3 Combination of 3D microscope and indentation results**

361 3D microscope and indentation data deconvolution phase assignments were combined  
 362 to reduce the variability of the identified phase properties. Comparing the indent natures  
 363 from the two first order techniques (3D microscope 3 groups identification vs 3 groups  
 364 hierarchical clustering), the indents with corresponding natures were considered as  
 365 representative of a given phase while the others were considered as non-reliable  
 366 information regarding the final application of this study, e.g. cement paste  
 367 characterization. This coupling may address the two main preoccupations of the first

368 order analysis: concerning numerical clustering this method can effectively provide a  
369 supplementary information about the nature of the indents and, concerning optical  
370 clustering, the method can considerably decrease the risk of false identification (either  
371 due to the operator or to the image precision) by selecting clusters of indents with close  
372 micromechanical properties.

373 From a visual inspection of the spatial repartition of the nature of the indents in one of  
374 the worst cases (Fig. 9), it should be observed that there is a huge proportion of  
375 noncorresponding indent natures (yellow squares). Indeed, when comparing 3 groups  
376 from 3D microscope identification and 3 groups from data deconvolution, around 35%  
377 of indents nature do not correspond between the two analysis, while this proportion is  
378 usually around 25% for the comparison between 3 groups from 3D microscope and 2  
379 groups from data deconvolution. A majority of noncorresponding indents are located in  
380 sand grains or at their periphery and this is the reason explaining why there is less error  
381 using 2 groups data from deconvolution data: data points numerically identified as  
382 belonging to the intermediate group were mostly visually identified as sand grains and  
383 not sand grain – cement paste interface. Only a very few indents were identified as  
384 interfaces by combining the two methods which means that groups identified by  
385 clustering algorithms with intermediate properties are not necessarily different phases  
386 (here sand grain – cement paste interface). Moreover, the variability of sand grain  
387 properties could also be visualized as for some sand grains almost all indents are  
388 corresponding ones, while for others, probably with smaller hardness, indents are  
389 mostly noncorresponding ones (identified as sand for one analysis, interface for the  
390 other).

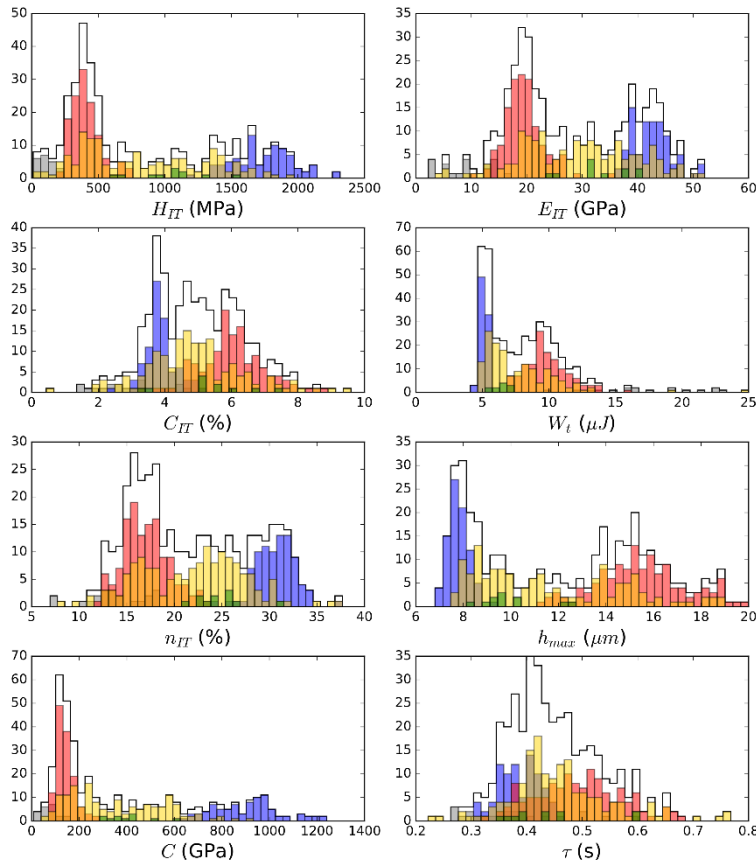


391

392 **Fig. 9.** Indents location and nature of specimen MD-257kGy-S3 comparing 3D  
393 microscope image analysis and 3 groups hierarchical data deconvolution (paste in red,  
394 cement paste - sand grain interface in green, pure sand in blue, void in black and indents  
395 with noncorresponding natures between the two analyses in yellow).

396

397 A detailed analysis of the microindentation output variables through histograms (Fig.  
398 10) reveals that noncorresponding indents are mainly the ones with intermediate  
399 properties as predicted by the visual observation. Interestingly, the initial goal of this  
400 comparison method seems to have been achieved: cement paste and sand distributions  
401 are tightened and do not overlap for Young's modulus, hardness and creep modulus.  
402 Moreover, some of the extreme values are filtered out. Thus, the comparison of  
403 numerical data deconvolution and optical data clustering efficiently reduces the  
404 uncertainties concerning phase identification because of the complementarity between  
405 the two methods.



407

408 **Fig. 10.** Histograms of distributions of the indentation output variables of specimen  
 409 MD-257kGy-S3 after the combined use of numerical and clustering and image analysis.  
 410 Total distribution is represented by the continuous black line, distributions of the phases  
 411 are colored in red (cement paste), blue (sand grains), green (sand grain – cement pastes  
 412 interface). The distribution of noncorresponding indents is represented in yellow.

413

#### 414 **3.4 Creep properties of $\gamma$ -irradiated mortar specimens**

415 Using the method described in the previous paragraphs, cement paste properties of  
 416 irradiated and control mortar specimens were compared. Tables 2 to 4 summarize the  
 417 indentation outputs associated with hierarchical clustering, 3D-microscope image  
 418 analysis and the method coupling numerical indentation data clustering and 3D-  
 419 microscope image analysis. As explained, the main interest of the technique is to reduce

420 the variability of the indentation outputs attributed to one phase, here the cement paste.  
421 This objective is achieved for most of the outputs as the variances of the outputs  
422 variables distributions in Table 4 are smaller than the corresponding ones on Table 2  
423 and 3 both on individual specimens and on the two series merging data from the 3  
424 specimens per series. Moreover, mean values of hardness, Young's modulus, creep  
425 parameter are smaller on Table 4 because some data points with intermediate properties  
426 were filtered out comparing numerical clustering and optical clustering.

427 One may finally observe that it is rather difficult to draw some conclusions on the  
428 evolution of the output variables due to irradiations from these data as the standard error  
429 (square-root of the variance) is close or greater than the difference between the two  
430 series. Thus, indentation outputs were grouped together whether they belong to  
431 irradiated specimens or not. The merged data is represented on Fig. 11. Analyzing non-  
432 diagonal graphics, one may observe that data points are rather well concentrated and  
433 dispersion limited. On diagonal probability distributions (PDF), a clear shift of  $C$  due to  
434 irradiations can be observed towards greater values while  $\tau$  decreases. Indentation  
435 hardness also seems to be affected, though statistical analysis is necessary to conclude  
436 concerning a possible influence of irradiations.

437

438 **Table 2.** Indentation outputs for cement paste indents identified using hierarchical  
 439 clustering (means and variances in brackets).

	HM (MPa)	HIT (MPa)	EIT (GPa)	CIT (%)	Wt ( $\mu$ J)	nIT (%)	hmax ( $\mu$ m)	C (GPa)	$\tau$ (s)
MD-257kGy-I1	377.4 (5424)	402.7 (6192)	19.5 (5.2)	5.16 (1.22)	10.2 (2.0)	16.7 (4.2)	15.40 (2.30)	173 (1111)	0.384 (0.005)
MD-257kGy-I2	432.0 (13035)	466.6 (16610)	21.0 (15.5)	5.20 (1.51)	9.3 (2.8)	18.1 (8.1)	14.54 (3.30)	197 (3534)	0.416 (0.007)
MD-257kGy-I3	438.8 (16321)	478.8 (22917)	21.3 (28.2)	5.04 (1.02)	9.2 (2.8)	19.0 (14.9)	14.46 (3.92)	210 (8623)	0.447 (0.005)
MD-257kGy-S1	396.9 (9088)	415.4 (10205)	20.2 (8.4)	6.00 (1.29)	10.1 (2.4)	16.7 (6.2)	15.26 (3.13)	149 (1006)	0.465 (0.005)
MD-257kGy-S2	369.3 (6869)	395.2 (8737)	19.9 (12.5)	4.99 (1.89)	9.7 (3.0)	17.5 (10.5)	15.58 (2.79)	182 (4653)	0.426 (0.006)
MD-257kGy-S3	416.1 (16467)	441.0 (20063)	20.8 (18.1)	5.77 (1.43)	9.7 (3.2)	17.3 (7.4)	15.01 (4.34)	165 (3481)	0.481 (0.007)
MD-257kGy-I	421.8 (13019)	456.2 (17314)	20.7 (18.2)	5.13 (1.27)	9.5 (2.7)	18.1 (10.4)	14.71 (3.43)	196 (4998)	0.420 (0.006)
MD-257kGy-S	396.2 (12102)	420.2 (14600)	20.4 (14.4)	5.55 (1.73)	9.8 (3.0)	17.2 (8.3)	15.25 (3.62)	168 (3539)	0.459 (0.007)

440

441 **Table 3.** Indentation outputs for cement paste indents identified using 3D-microscope  
 442 image analysis (means and variances in brackets).

	HM (MPa)	HIT (MPa)	EIT (GPa)	CIT (%)	Wt ( $\mu$ J)	nIT (%)	hmax ( $\mu$ m)	C (GPa)	$\tau$ (s)
MD-257kGy-I1	440.8 (19742)	476.8 (27060)	21.2 (12.9)	5.24 (1.29)	9.4 (2.9)	18.0 (11.9)	14.50 (3.92)	199 (4667)	0.400 (0.005)
MD-257kGy-I2	434.1 (17383)	468.9 (23191)	20.6 (16.4)	5.33 (1.20)	9.4 (3.0)	17.9 (8.3)	14.60 (3.82)	192 (4943)	0.425 (0.007)
MD-257kGy-I3	431.9 (15769)	464.6 (21090)	20.4 (20.5)	5.63 (1.15)	9.3 (2.2)	18.6 (12.4)	14.64 (3.50)	177 (4922)	0.478 (0.007)
MD-257kGy-S1	480.2 (22752)	509.0 (32818)	22.4 (15.9)	6.39 (0.97)	9.1 (2.3)	18.1 (10.6)	14.01 (3.09)	166 (5071)	0.558 (0.013)
MD-257kGy-S2	412.5 (28845)	443.9 (42071)	20.3 (18.6)	5.44 (1.62)	9.6 (2.8)	17.6 (9.7)	15.17 (4.73)	180 (8569)	0.435 (0.005)
MD-257kGy-S3	402.8 (16326)	425.0 (20613)	20.0 (18.6)	6.00 (0.96)	9.7 (3.2)	17.3 (8.1)	15.29 (4.33)	151 (3661)	0.495 (0.007)
MD-257kGy-I	435.7 (17592)	470.2 (23734)	20.8 (16.5)	5.40 (1.24)	9.4 (2.7)	18.2 (10.9)	14.58 (3.74)	190 (4898)	0.434 (0.007)
MD-257kGy-S	432.2 (23588)	459.5 (32752)	20.9 (18.8)	5.95 (1.32)	9.5 (2.8)	17.7 (9.6)	14.82 (4.36)	165 (5814)	0.497 (0.011)

443

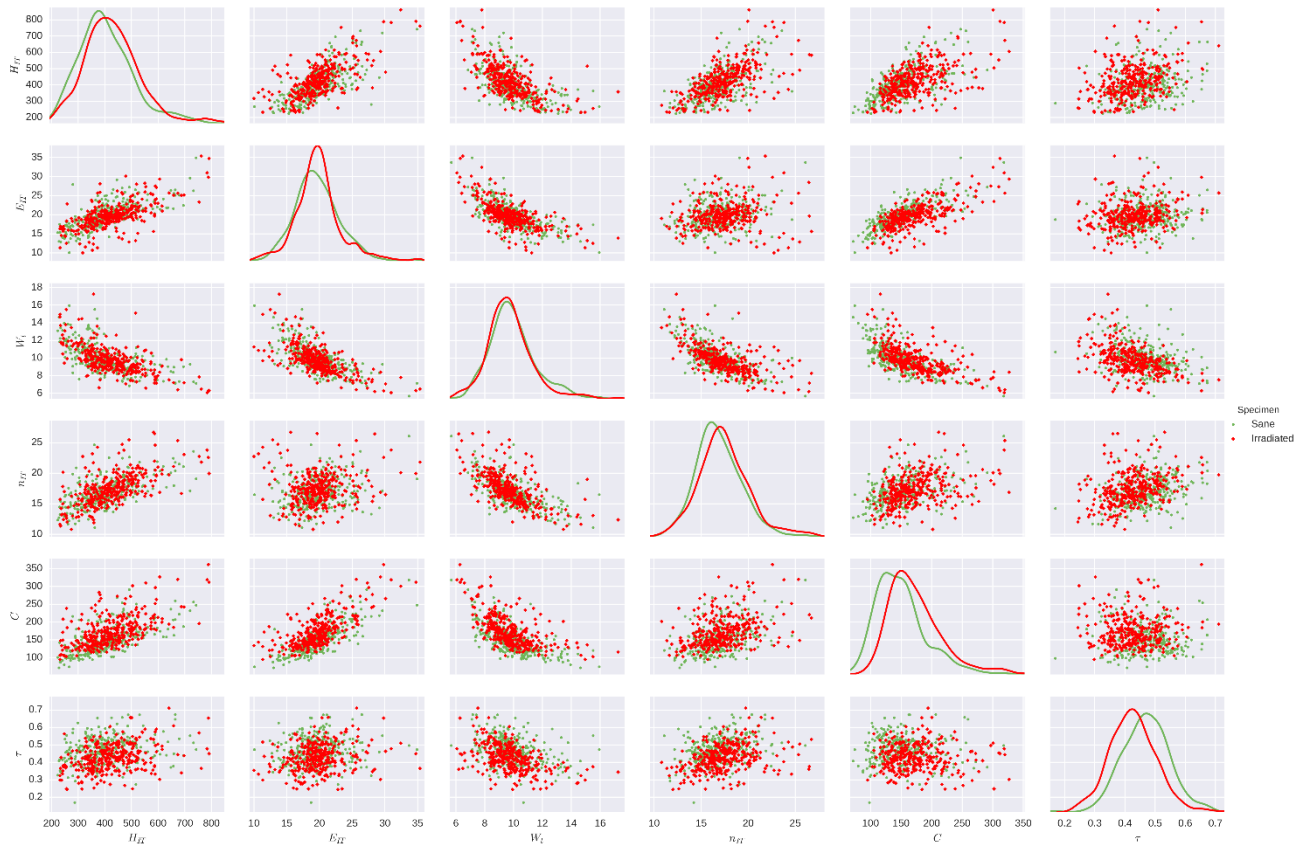
444 **Table 4.** Indentation outputs for cement paste indents identified using the proposed  
 445 method coupling numerical clustering and image analysis (means and variances in  
 446 brackets).

	HM (MPa)	HIT (MPa)	EIT (GPa)	CIT (%)	Wt ( $\mu$ J)	nIT (%)	hmax ( $\mu$ m)	C (GPa)	$\tau$ (s)
MD-257kGy-I1	376.0 (5267)	400.6 (5997)	19.4 (4.8)	5.25 (1.21)	10.2 (2.1)	16.6 (4.6)	15.44 (2.26)	168 (919)	0.391 (0.004)
MD-257kGy-I2	416.9 (11407)	448.1 (14084)	20.2 (12.8)	5.33 (1.22)	9.6 (2.8)	17.6 (6.6)	14.79 (3.20)	183 (2896)	0.429 (0.007)
MD-257kGy-I3	397.8 (8279)	428.1 (11073)	19.7 (19.3)	5.35 (0.91)	9.6 (2.1)	18.1 (12.2)	15.09 (2.79)	174 (4012)	0.454 (0.004)
MD-257kGy-S1	411.2 (8037)	428.4 (9145)	20.4 (7.9)	6.33 (0.77)	10.2 (2.4)	16.4 (4.8)	15.00 (2.59)	144 (773)	0.476 (0.004)
MD-257kGy-S2	372.3 (9381)	395.0 (11590)	19.6 (13.0)	5.40 (1.63)	9.9 (2.5)	16.9 (5.5)	15.63 (2.92)	162 (2310)	0.439 (0.005)
MD-257kGy-S3	387.5 (10432)	406.7 (12111)	19.5 (12.7)	6.03 (0.88)	9.9 (2.7)	17.0 (5.8)	15.48 (3.54)	142 (1247)	0.493 (0.006)
MD-257kGy-I	399.7 (8965)	428.8 (11226)	19.8 (12.7)	5.32 (1.12)	9.7 (2.5)	17.5 (8.1)	15.06 (2.87)	176 (2723)	0.427 (0.006)
MD-257kGy-S	386.0 (9739)	406.1 (11455)	19.7 (12.0)	5.85 (1.26)	9.9 (2.6)	16.9 (5.5)	15.45 (3.17)	150 (1639)	0.470 (0.006)

447

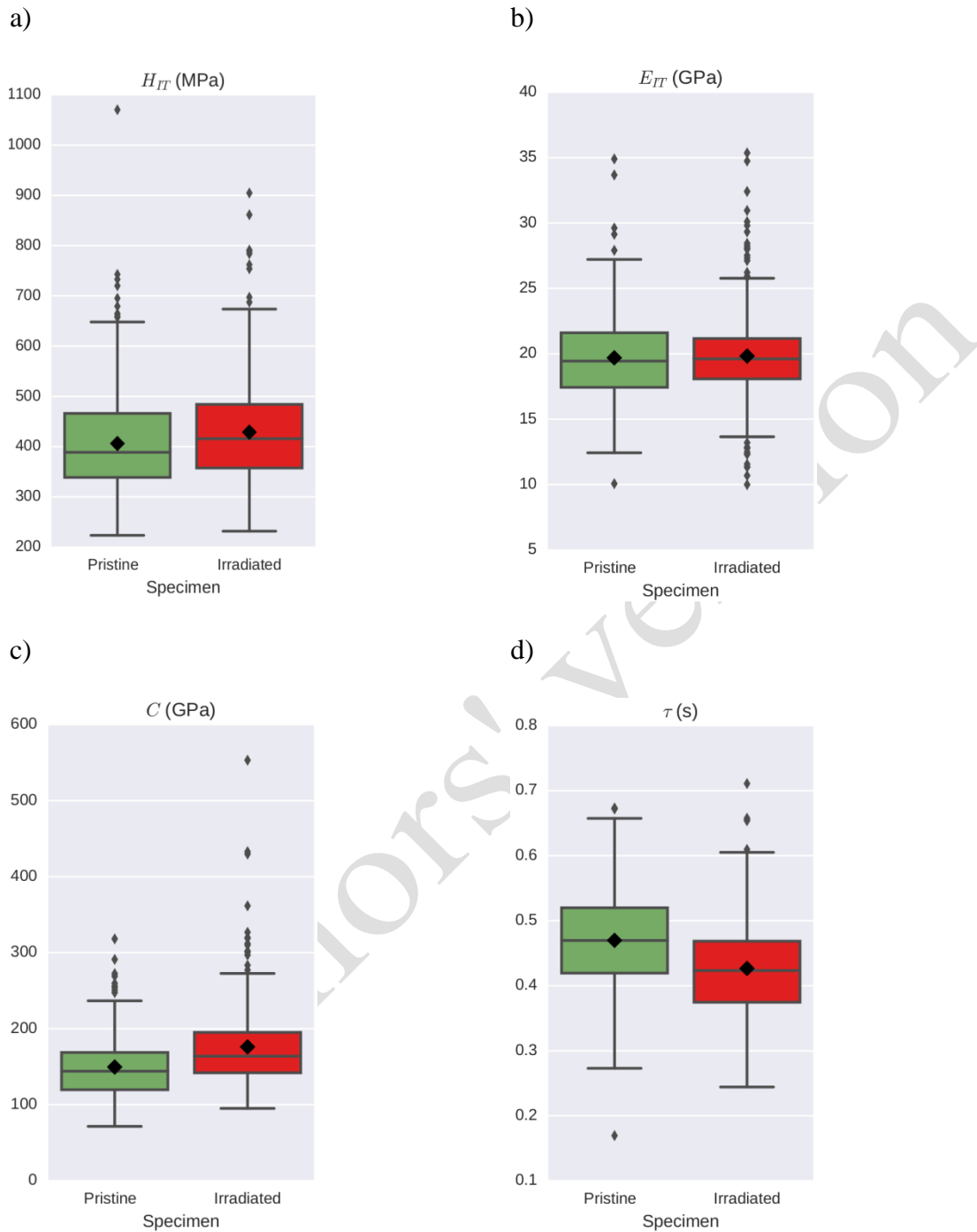
448 Statistical analysis was performed using Gnumeric software. Because normality of these  
 449 new distributions could not be guaranteed using normality algorithms and variances  
 450 could differ slightly, irradiated and control specimens data points were compared using  
 451 the Welch's t-test (mean comparison assuming normal distributed variables but  
 452 sufficiently robust to deal with non-normal samples if there are enough data points) and  
 453 Wilcoxon-Mann-Whitney test (median comparison without normality assumption) as a  
 454 verification both at a confidence level of 5%. There is no significant difference  
 455 concerning Young's moduli in agreement with the tables. After a total irradiated dose of  
 456 257 kGy, there is a significant increase of the creep modulus C of about 17% and a  
 457 significant decrease of indentation characteristic time  $\tau$  of about 9% comparing data  
 458 points obtained from the method herein presented. Box plots summarizing the results  
 459 are presented in Fig. 12. These proportions are similar to the ones computed from

460 hierarchical or 3D-microscope analysis outputs but may not be statistically different in  
 461 the latter cases, especially when data points are identified using 3D-microscope only.  
 462 Creep modulus increase is correlated with a slight indentation hardness increase of  
 463 about 6% which is significant for data points obtained using the coupled method.  
 464 Consequently,  $h_{\max}$  slightly decreases while  $n_{IT}$  slightly increases with irradiations. The  
 465 indentation energy  $W_t$  remains unchanged proving that only slight changes are  
 466 occurring.  
 467



468 **Fig. 11.** Scatter plot of indentation data points attributed to the cement paste by  
 469 coupling data deconvolution and image analysis for irradiated and control specimens  
 470 ( $H_{IT}$  is expressed in MPa,  $E_{IT}$  and  $C$  in GPa,  $n_{IT}$  in %,  $W_t$  in  $\mu$ J and  $\tau$  in s).  
 471

472



474 **Fig. 12.** Box plots of indentation data points attributed to the cement paste by coupling  
 475 data deconvolution and image analysis for irradiated and pristine specimens: a)  $H_{IT}$ , b)  
 476  $E_{IT}$ , c)  $C$  and d)  $\tau$ , Center horizontal line of the box represents the median value while  
 477 thick diamond stands for the mean value.

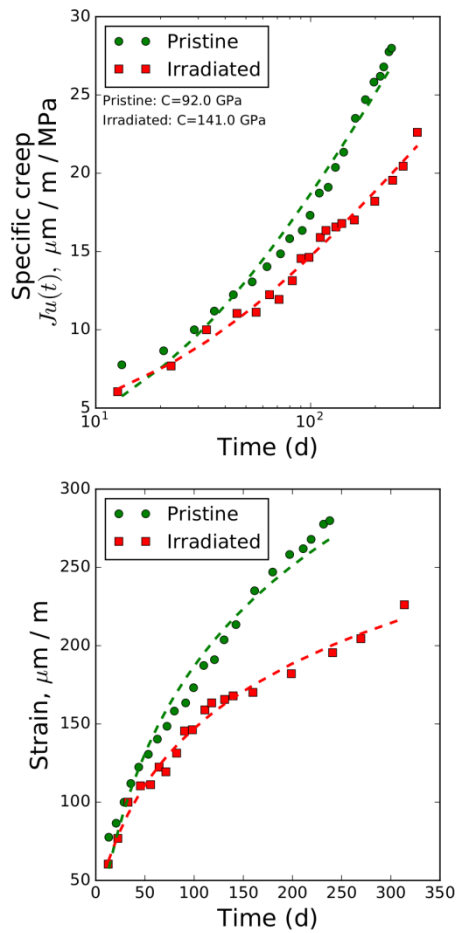
479 From our knowledge, these creep results are the first microindentation results  
 480 concerning irradiated concrete specimens. Therefore, it could be interesting to make a  
 481 comparison with the only macroscopic creep results under  $\gamma$ -irradiation reported a long  
 482 time ago [39] and illustrated as markers in Fig. 13. The experimental macroscopic  
 483 specific creep function was first fitted using a classic 3-parameters logarithmic law:

$$J_u(t) - \frac{1}{E_0} = \frac{\ln(t/\tau + 1)}{C} \quad (11)$$

484 This first fit led to an increase of the creep modulus of 74% (132 GPa for irradiated  
 485 sample and 76 GPa for control sample) and a decrease of  $\tau$  of around 49 % (47 d  
 486 vs 24d). Though the raw increases are dramatic and somehow affected by the lack of  
 487 experimental values compared to the number of parameters, this trend qualitatively  
 488 agrees with the microindentation results. In order to obtain more realistic creep modulus  
 489 variations, it has been decided to fit the experimental data using a two parameters law  
 490 written as:

$$J_u(t) - \frac{1}{E_0} = \frac{\ln(t/cste + 1)}{C} \quad (11)$$

491 Using a characteristic time *cste* of 25 d (same order of magnitude as the characteristic  
 492 time using a 3-parameters fit. but still a relatively small value regarding the dose  
 493 (around 70 kGy) at this time), this type of law correctly describe the creep behavior for  
 494 times greater than  $\tau$ . As illustrated in Fig. 13, the fit is acceptable for times greater than  
 495 approximately 40 d. When applied on the regression curves proposed by McDowall,  
 496 this fit leads to a more reasonable creep modulus increase of 53% after a total dose  
 497 820kGy in approximately 300 d (141 GPa for the irradiated specimen and 92 GPa for  
 498 the control specimen). This increase is around three times greater than the increase  
 499 measured by indentation after a total dose of 257 kGy.



500

501 **Fig. 13.** Comparison between experimental creep results from [39] (markers) and a 2-  
 502 parameters logarithmic fit (dashed line).

503

504 Therefore, in order to compare creep modulus' increase at similar total doses, we  
 505 performed 2-parameters fitting up to increasing doses with the assumption that  
 506 irradiation gradually affects cementitious materials. For this purpose, we approximated  
 507 the initial fit of the evolution of strain proposed by McDowall in order to feed the  
 508 algorithm with continuous data. Then logarithmic 2-parameters fitting was realized  
 509 between dose segments of growing sizes beginning by a first segment of [0 kGy,  
 510 20 kGy] and gradually increasing the size of the segment by 0.5 kGy. The general trend  
 511 of the optimization problem for the ratio of the creep modulus evolution assessment,  
 512 depending on time  $t$  and dose  $d$ , is summarized by eq. 12 where  $J'$  and  $J$  are the specific

513 creep function of the irradiated and control specimens. The resulting evolution of the  
 514 ratio between the creep moduli of irradiated concrete specimen and control specimen  
 515 over the total dose is illustrated in Fig. 14.

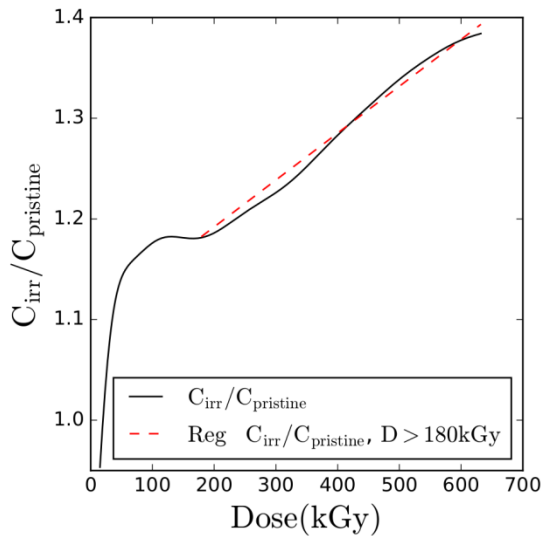
516

$$\frac{C_{Irr}(d)}{C_{sane}} = \frac{\min_{c,\tau=25d} \int_0^d J'_{exp}(t,d) - J'_{num}(t,d)}{\min_{c,\tau=25d} \int_0^d J'_{exp}(t) - J'_{num}(t)} \quad (12)$$

517

518 Because the effect of radiations is supposedly small at low doses, creep moduli ratio is  
 519 close to 1 for small segments and. because the effect of radiation increases with time the  
 520 ratio gradually increases. It is difficult to say whether the quick increase of the ratio  
 521 before 50-60 kGy is representative of the concrete behavior or if the fit reliability is  
 522 affected by the logarithmic function selected (irradiation times are close to the creep  
 523 characteristic time at low dosage). However, one may observe the ratio exhibits a quasi-  
 524 linear increase after 180 kGy (doses at which time  $\geq 3 \times$  creep characteristic time). A  
 525 linear regression with a correlation coefficient of 0.994 is proposed after 180 kGy. From  
 526 this regression, it can be stated that the increase rate is of  $5 \times 10^{-2}\%$  / kGy, which leads,  
 527 considering and initial creep modulus of around 100 GPa, to a rate of 50 GPa/MGy. For  
 528 a dose of 257 kGy, the increase of the creep modulus from this method is around 20%  
 529 which is in good agreement with the increase calculated from the microindentation  
 530 experiment.

531



532

533 **Fig. 14.** Evolution of the ration between creep moduli calculated for irradiated and  
 534 control concrete specimens from [39] relatively to the final dose considered for a 2-  
 535 parameters fitting logarithmic law.

536

#### 537 **4. Conclusion and perspectives**

538 In this study, the potential of coupling indentation and optical microscopy for  
 539 heterogenous materials characterization has been demonstrated. A novel method has  
 540 been introduced to reduce the variability of the micromechanical properties associated  
 541 to an indented phase. This method relies on the comparison of the nature of indents  
 542 numerically predicted by statistical indentation data deconvolution and by 3D-optical  
 543 microscope image analysis. This method robustly counteracts the uncertainty of  
 544 numerical clustering methods by introducing optical information. In our study, the data  
 545 points cluster of interest generated by the method associated with cement paste likely  
 546 exhibits a normal distribution and a systematic reduced variance compared to each of  
 547 the technique alone. This herein described method could be applied to a wide range of  
 548 materials and studies.

549 The proposed method was successfully applied to the assessment of micro-mechanical  
 550 properties of  $\gamma$ -irradiated mortar specimens. The method led to the identification of the

551 cement paste elasto-plastic parameters affected by irradiation at relatively low  
552 cumulated dose of 257 kGy. It has been found out that creep modulus  $C$  significantly  
553 increases by around 17% and indentation characteristic time  $\gamma$  significantly decreases by  
554 around 9% after irradiation. The creep modulus increase is correlated with a slight  
555 increase of the indentation hardness  $H_{IT}$  and of the proportion of the elastic response  
556 relatively to the total energy  $n_{IT}$ . On the other hand, Young's modulus of irradiated  
557 specimens does not significantly differ from the one of control specimens.  
558 These micro-mechanical observations agree with the only macroscopic uniaxial  
559 compressive creep measurements under  $\gamma$ -irradiation published to our knowledge [39].  
560 Using a logarithmic dose-dependant fit of the specific creep function proposed in this  
561 study, it can be calculated that the creep modulus increases and the creep characteristic  
562 time decreases leading to less creep of the irradiated samples. Then a reverse analysis  
563 was proposed to quantify the evolution of the irradiated vs pristine creep moduli ratio  
564 with the time increasing  $\gamma$ -dose. Although supplementary similar experiments should be  
565 carried out at both microscale and macroscale with various dose rates, the creep  
566 modulus appears to linearly increase with the  $\gamma$ -dose for doses between 180 and  
567 700 kGy.

568

### 569 **Acknowledgments**

570 The authors gratefully acknowledge the financial support provided for this study by  
571 Tractebel Engineering. Special thanks are due to Xavier Bourbon (ANDRA) for  
572 instructive discussions. This work has been supported in part by a grant from the French  
573 National Agency for Research called "Investissements d'Avenir". Equipex ArronaxPlus  
574 n°ANR-11-EQPX-0004.

575

576 **References**

- 577 [1] P. Trtik and P. J. M. Bartos. Micromechanical properties of cementitious  
578 composites. *Materials and Structures*, 32(5):388–393, 1999.
- 579 [2] P. Acker. Micromechanical analysis of creep and shrinkage mechanisms. In  
580 *Creep, shrinkage and durability mechanics of concrete and other quasi-brittle*  
581 *materials. (Proceedings of ConCreep6)*, 2001.
- 582 [3] K. Velez, S. Maximilien, D. Damidot, G. Fantozzi, and F. Sorrentino.  
583 Determination by nanoindentation of elastic modulus and hardness of pure constituents  
584 of portland cement clinker. *Cement and Concrete Research*, 31(4):555 – 561, 2001.
- 585 [4] G. Constantinides, F.-J. Ulm, and K. Van Vliet. On the use of nanoindentation  
586 for cementitious materials. *Materials and Structures*, 36(3):191–196, 2003.
- 587 [5] G. Constantinides and F.-J. Ulm. The effect of two types of c-s-h on the  
588 elasticity of cement-based materials: Results from nanoindentation and  
589 micromechanical modeling. *Cement and Concrete Research*, 34:67–80, 2004.
- 590 [6] J. J. Chen, L. Sorelli, M. Vandamme, F.-J. Ulm, and G. Chanvillard. A coupled  
591 nanoindentation/sem-eds study on low water/cement ratio portland cement paste:  
592 Evidence for c-s-h/ca(oh)<sub>2</sub> nanocomposites. *Journal of the American Ceramic Society*,  
593 93(5):1484–1493, 2010.
- 594 [7] M. Vandamme and F.-J. Ulm. Nanoindentation investigation of creep properties  
595 of calcium silicate hydrates. *Cement and Concrete Research*, 52:38 – 52, 2013.
- 596 [8] W.C. Oliver and G.M. Pharr. An improved technique for determining hardness  
597 and elastic modulus using load and displacement sensing indentation experiments.  
598 *Journal of Materials Research*, 7:1564–1583, 1992.

- 599 [9] F.-J. Ulm, M. Vandamme, C. Bobko, J.A. Ortega, K. Tai, and C Ortiz. Statistical  
600 indentation techniques for hydrated nanocomposites: Concrete, bone, and shale. *Journal*  
601 *of the American Ceramic Society*, 90:2677–2692, 2007.
- 602 [10] L. Sorelli, G. Constantinides, F.-J. Ulm, and F. Toutlemonde. The nano-  
603 mechanical signature of ultra high performance concrete by statistical nanoindentation  
604 techniques. *Cement and Concrete Research*, 38(12):1447 – 1456, 2008.
- 605 [11] C. Hu, Y. Gao, Y. Zhang, and Z. Li. Statistical nanoindentation technique in  
606 application to hardened cement pastes: Influences of material microstructure and  
607 analysis method. *Construction and Building Materials*, 113:306 – 316, 2016.
- 608 [12] P. Trtik, B. Münch, and P. Lura. A critical examination of statistical  
609 nanoindentation on model materials and hardened cement pastes based on virtual  
610 experiments. *Cement and Concrete Composites*, 31(10):705 – 714, 2009.
- 611 [13] F.-J. Ulm, M. Vandamme, H. M. Jennings, J. Vanzo, M. Bentivegna, K. J.  
612 Krakowiak, G. Constantinides, C. P. Bobko, and K. J. Van Vliet. Does microstructure  
613 matter for statistical nanoindentation techniques? *Cement and Concrete Composites*,  
614 32(1):92 – 99, 2010.
- 615 [14] D. Davydov, M. Jirásek, and L. Kopecký. Critical aspects of nano-indentation  
616 technique in application to hardened cement paste. *Cement and Concrete Research*,  
617 41(1):20 – 29, 2011.
- 618 [15] P. Lura, P. Trtik, and B. Münch. Validity of recent approaches for statistical  
619 nanoindentation of cement pastes. *Cement and Concrete Composites*, 33(4):457 – 465,  
620 2011.
- 621 [16] P. Mondal, S. P. Shah, and L. Marks. A reliable technique to determine the local  
622 mechanical properties at the nanoscale for cementitious materials. *Cement and Concrete*  
623 *Research*, 37(10):1440 – 1444, 2007.

- 624 [17] J. J. Hughes and P. Trtik. Micro-mechanical properties of cement paste  
625 measured by depth-sensing nanoindentation: a preliminary correlation of physical  
626 properties with phase type. *Materials Characterization*, 53:223 – 231, 2004. EMABM  
627 2003: 9th Euroseminar on Microscopy Applied to Building Materials.
- 628 [18] C. Hu and Z. Li. Micromechanical investigation of portland cement paste.  
629 *Construction and Building Materials*, 71:44 – 52, 2014.
- 630 [19] W. Zhu, J. J. Hughes, N. Bicanic, and Chris J. Pearce. Nanoindentation mapping  
631 of mechanical properties of cement paste and natural rocks. *Materials Characterization*,  
632 58:1189 – 1198, 2007. 10th Euroseminar on Microscopy Applied to Building Materials  
633 (EMABM).
- 634 [20] S. Zhao and W. Sun. Nano-mechanical behavior of a green ultra-high  
635 performance concrete. *Construction and Building Materials*, 63:150 – 160, 2014.
- 636 [21] M. Vandamme, F.-J. Ulm, and P. Fonollosa. Nanogranular packing of C-S-H at  
637 substochiometric conditions. *Cement and Concrete Research*, 40(1):14 – 26, 2010.
- 638 [22] A. B. Nichols and D. A. Lange. 3d surface image analysis for fracture modeling  
639 of cement-based materials. *Cement and Concrete Research*, 36(6):1098 – 1107, 2006.
- 640 [23] T. Ficker, D. Martisek, and H. M. Jennings. Roughness of fracture surfaces and  
641 compressive strength of hydrated cement pastes. *Çement and Concrete Research*,  
642 40(6):947 – 955, 2010.
- 643 [24] B. Hilloulin, J.-B. Legland, E. Lys, O. Abraham, A. Loukili, F. Grondin, O.  
644 Durand, and V. Tournat. Monitoring of autogenous crack healing in cementitious  
645 materials by the nonlinear modulation of ultrasonic coda waves, 3d microscopy and x-  
646 ray microtomography. *Construction and Building Materials*, 123:143 – 152, 2016.

- 647 [25] Q. Zhang, R. Le Roy, M. Vandamme, and B. Zuber. Long-term creep properties  
648 of cementitious materials: Comparing microindentation testing with macroscopic  
649 uniaxial compressive testing. *Cement and Concrete Research*, 58:89 – 98, 2014.
- 650 [26] M. Irfan-ul-Hassan, B. Pichler, R. Reihnsner, and Ch. Hellmich. Elastic and creep  
651 properties of young cement paste, as determined from hourly repeated minute-long  
652 quasi-static tests. *Cement and Concrete Research*, 82:36 – 49, 2016.
- 653 [27] D.-T. Nguyen, R. Alizadeh, J. J. Beaudoin, P. Pourbeik, and L. Raki.  
654 Microindentation creep of monophasic calcium-silicate-hydrates. *Cement and Concrete*  
655 *Composites*, 48:118 – 126, 2014.
- 656 [28] J. Frech-Baronet, L. Sorelli, and J.-P. Charron. New evidences on the effect of  
657 the internal relative humidity on the creep and relaxation behaviour of a cement paste by  
658 micro-indentation techniques. *Cement and Concrete Research*, 91:39 – 51, 2017.
- 659 [29] K.G. Field, I. Remec, and Y. Le Pape. Radiation effects in concrete for nuclear  
660 power plants - part i: Quantification of radiation exposure and radiation effects. *Nuclear*  
661 *Engineering and Design*, 282:126 – 143, 2015.
- 662 [30] Y. Le Pape, K.G. Field, and I. Remec. Radiation effects in concrete for nuclear  
663 power plants, part ii: Perspective from micromechanical modeling. *Nuclear Engineering*  
664 *and Design*, 282:144 – 157, 2015.
- 665 [31] A. Giorla, M. Vaitová, Y. Le Pape, and P. Štemberk. Meso-scale modeling of  
666 irradiated concrete in test reactor. *Nuclear Engineering and Design*, 295:59 – 73, 2015.
- 667 [32] H. K. Hilsdorf, J. Kropp, and H. J. Koch. The effects of nuclear radiation on the  
668 mechanical properties of concrete. Technical report, ACI SP-55, 1978.
- 669 [33] ANDRA. Dossier 2005 argile, architecture and management of a geological  
670 repository. Technical report, ANDRA, 2005.

- 671 [34] P. Soo and L. M. Milian. The effect of gamma radiation on the strength of  
672 portland cement mortars. *Journal of Materials Science Letters*, 20(14):1345–1348,  
673 2001.
- 674 [35] F. Vodák, K. Trtík, V. Sopko, O. Kapicková, and P. Demo. Effect of  $\gamma$  -  
675 irradiation on strength of concrete for nuclear-safety structures. *Cement and Concrete*  
676 *Research*, 35(7):1447 – 1451, 2005.
- 677 [36] O. Kontani, Y. Ichikawa, A. Ishizawa, M. Takizawa, and O. Sato. Irradiation  
678 effects on concrete structures. In *International Symposium on the Ageing Management*  
679 *& Maintenance of Nuclear Power Plants*, 2010.
- 680 [37] O. Kontani, S. Sawada, I. Maruyama, M. Takizawa, and O. Sato. Evaluation of  
681 irradiation effects on concrete structure - gamma - ray irradiation test on cement paste.  
682 In *Proceedings of the ASME 2013 Power Conference (POWER2013), July 29-August 1,*  
683 *2013, Boston, Massachusetts, USA*, 2013.
- 684 [38] A. Lowinska-Kluge and P. Piszora. Effect of gamma irradiation on cement  
685 composites observed with XRD and SEM methods in the range of radiation dose 0 -  
686 1409 MGy. *Acta Physica Polonica, A*, 114:399 – 411, 2008.
- 687 [39] D. McDowall. The effects of gamma radiation on the creep properties of  
688 concrete. In *Proceedings of the Information Exchange Meeting on 'Results of Concrete*  
689 *Irradiation Programs', EUR 4751 f-e, Commission des Communautés Européennes,*  
690 *Brussels, Belgium*, 1971.
- 691 [40] R.L. Grossman, C. Kamath, P. Kegelmeyer, V. Kumar, and R. Namburu. *Data*  
692 *Mining for Scientific and Engineering Applications*. Springer US, 2001.
- 693 [41] Krishna Rajan. Materials informatics. *Materials Today*, 8(10):38 – 45, 2005.
- 694 [42] J.H. Koo. *Polymer Nanocomposites: Processing, Characterization, and*  
695 *Applications*. McGraw-Hill, New York, 2006.

- 696 [43] S. K. Barai. Data mining applications in transportation engineering. *Transport*,  
697 18(5):216–223, 2003.
- 698 [44] F. Vodák, V. Vydra, K. Trtík, and O. Kapiccková. Effect of gamma irradiation  
699 on properties of hardened cement paste. *Materials and Structures*, 44:101 – 107, 2011.
- 700 [45] M. Miller, C. Bobko, M. Vandamme, and F.-J. Ulm. Surface roughness criteria  
701 for cement paste nanoindentation. *Cement and Concrete Research*, 38(4):467 – 476,  
702 2008.
- 703
- 704

Authors' version